RESEARCH ARTICLE

ADVANCED
PHYSICS
RESEARCH
Open Access

www.advphysicsres.com

Observation of the Chiral Soliton Lattice above Room Temperature

R. Brearton, S. H. Moody, L. A. Turnbull, P. D. Hatton, A. Štefančič, G. Balakrishnan, G. van der Laan, and T. Hesjedal*

Magnetic chiral soliton lattices (CSLs) emerge from the helical phase in chiral magnets when magnetic fields are applied perpendicular to the helical propagation vector, and they show great promise for next-generation magnetic memory applications. These one-dimensional structures are previously observed at low temperatures in samples with uniaxial symmetry. Here, it is found that in-plane fields are the key to stabilizing the CSL in cubic $Co_8Zn_{10}Mn_2$ over the entire temperature range from 15 K to below the Curie temperature (365 K). Using small-angle resonant elastic X-ray scattering, it is observed that the CSL is stabilized with an arbitrary in-plane propagation vector, while its thin plate geometry plays a deciding role in the soliton wavelength as a function of applied field. This work paves the way for high temperature, real world applications of soliton physics in future magnetic memory devices.

1. Introduction

While magnetic skyrmions are two-dimensional (2D) topological field configurations with many proposed applications in spintronics devices,[1,2] magnetic solitons represent a 1D topological field configuration, where a single 2π twist of the spin chain cannot be smoothly deformed into the field-polarized state, relevant to high energy physics and chiral magnets alike.[3–6] As a result, magnetic solitons have been the subject of some interest as candidate information carriers themselves, where the state of the spin chain (either having, or lacking, a twist) can represent the state of a bit of information.[7,8] Like skyrmions, they can be driven with ultralow current densities,[9–11] however, unlike skyrmions, they can be freely created[12] and straightforwardly electrically read-out, resulting from Bragg scattering of the conduction electrons showing discrete steps.[13,14] Magnetic solitons may therefore be suitable for racetrack memory applications, spin phase electronics,[15] and in magnon-driven devices.[16]

In the presence of a sizable external magnetic field, helimagnetic configurations unfortunately tend to align their *k*-vectors with the field to form the more stable conical state. The magnetic chiral soliton lattice (CSL) has been long understood theoretically to be a consequence of applying a field perpendicular to the propagation vector of the helical phase.[3,17,18] However, measurements of the CSL are relatively scarce. In fact, despite their theoretical prediction by Igor Dzyaloshinskii in 1964,[3] the magnetic soliton lattice was only first observed in a sample of $CrNb_3S_6$ in 2012.[7]

The helical phase arises in chiral magnets, many of which have cubic symmetry, as well as more recently in systems with hexagonal symmetry.[19] Particularly since the discovery of the magnetic skyrmion lattice state in these systems,[20] their magnetic phase diagrams have been widely studied. Typically, when one applies a large magnetic field (large enough that the Zeeman free energy density becomes comparable to the exchange and Dzyaloshinskii–Moriya (DM) free energy densities), the cone phase will form; the helices in the material will reorient such that their propagation vector lies parallel to the applied magnetic field, so that their spins can cant toward the applied field to decrease their Zeeman energy. The presence (and relatively low energy cost) of the cone phase makes the observation of the chiral soliton lattice difficult, as they appear in the same region of the magnetic phase diagram.

The situation changes in $CrNb_3S_6$, which has a single helical axis in its unit cell that pins helimagnetic textures, forcing them

R. Brearton, G. van der Laan, T. Hesjedal
Diamond Light Source
Harwell Science and Innovation Campus
Didcot OX11 0DE, UK
E-mail: thorsten.hesjedal@physics.ox.ac.uk

R. Brearton, T. Hesjedal
Department of Physics
Clarendon Laboratory
University of Oxford
Oxford OX1 3PU, UK

S. H. Moody, L. A. Turnbull, P. D. Hatton
Department of Physics
Durham University
Durham DH1 3LE, UK

A. Štefančič, G. Balakrishnan
Department of Physics
University of Warwick
Coventry CV4 7AL, UK

**ADVANCED
SCIENCE NEWS**

www.advancedsciencenews.com

**ADVANCED
PHYSICS
RESEARCH**

www.advphysicsres.com

to propagate along that direction.[7,21,22] Here, the CSL was stabilized by applying a field perpendicular to the principal axis of $CrNb_3S_6$, allowing for the state to be observed at temperatures under 127 K. In Cu_2OSeO_3, which has a chiral cubic structure, the chiral soliton lattice has also been observed.[23] This was possible by straining the Cu_2OSeO_3 crystal uniaxially. This strain breaks the cubic symmetry and stabilizes the chiral soliton lattice with a propagation vector parallel to the strain direction. So, due to the cubic symmetry of the underlying Cu_2OSeO_3 crystal, it was necessary to break that symmetry to stabilize the chiral soliton lattice.

Cubic chiral magnets have been the focus of attention for the exploration of topological magnetism ever since the discovery of magnetic skyrmions in MnSi.[20] In related itinerant B20 materials (non-centrosymmetric space group $P2_13$), such as (Fe,Co)Si[24] and FeGe,[25] skyrmions have been discovered shortly thereafter. With a T_C of ≈ 280 K, FeGe held the noncentrosymmetric bulk crystal record until the discovery of Co-Zn-Mn with a T_C more than 450 K in 2015,[26] which is ideally suited for skyrmion-based spintronics devices.[2] This intermetallic with a $Co_xZn_yMn_z$ (with the integer numbers $x + y + z = 20$) stoichiometry and β-Mn structure[27] also belongs to a cubic chiral space group ($P4_132$ or $P4_332$). The T_C of $Co_{10}Zn_{10}$ is the highest in the series (>460 K), and it decreases with increasing Mn content,[26] yet still above room temperature for $Co_8Zn_8Mn_4$ (and below room temperature for larger Mn content). Apart from the observation of skyrmions, $Co_xZn_yMn_z$ proved to be a fertile ground for the exploration of square meron lattices[28] and Bloch points at the end of skyrmion strings in nanowires,[29] and they are well-known for the rich variety of skyrmion phases existing far from equilibrium.[30] $Co_xZn_yMn_z$ chiral magnets have a rich phase diagram, which is witness to the different competing contributions to its free energy, i.e., DM-coupled Co moments giving rise to chiral magnetism, magnetic frustration stemming from antiferromagnetic Mn spin correlations, a temperature and Mn composition varying magnetic anisotropy,[31] and compositional disorder.[30]

Here, using transmission resonant elastic X-ray scattering (T-REXS), we demonstrate the robust formation of the CSL in the high-temperature chiral cubic magnet $Co_8Zn_{10}Mn_2$. By applying an in-plane field normal to the propagation vector of the helical phase, the CSL state can be stabilized in a thin plate of $Co_8Zn_{10}Mn_2$ in an extremely wide phase pocket between 15 and 344 K ($T_C \approx 365$ K), and up to 140 mT. The CSL's in-plane propagation vector is controlled by the applied field direction, while the soliton wavelength is affected by the sample shape. The topological protection of the CSL is further evidenced by its continued existence in the presence of defects, which introduce domains far from T_C but which do not affect their robustness.

2. Results and Discussion

2.1. Challenges in Observing the Chiral Soliton Lattice

The issue of observing the CSL can be readily understood by inspecting the solutions to the Euler–Lagrange equations of a simple toy model of the magnetic free energy containing only Dzyaloshinskii–Moriya, exchange and Zeeman interactions terms, given by [32]

$$E = \iiint \left[A(\nabla\mathbf{m})^2 + D\mathbf{m} \cdot (\nabla \times \mathbf{m}) - \mathbf{m} \cdot \mathbf{B} \right] d^3x \quad (1)$$

where A is the exchange coupling constant, D tunes the strength of the Dzyaloshinskii–Moriya interaction, $\mathbf{B}$ is the magnetic flux density, and $\mathbf{m}$ is the magnetization, whose structure we would like to investigate. Consider also a general helicoidal ansatz

$$\mathbf{m} = \left[\cos\psi(z)\cos\zeta, \sin\psi(z)\cos\zeta, \sin\zeta \right] \quad (2)$$

where the propagation vector of the helicoid has been used to orient the z-axis, ζ denotes a tilt angle towards the propagation vector, and the function $\psi(z)$ describes the internal structure of the helicoid. Assuming that the functional Equation (1) is valid, any magnetization structure that can be observed in an experiment must extremize (and, preferably, locally minimize) Equation (1). Substituting the ansatz Equation (2) into Equation (1) and inspecting the Euler-Lagrange equations when $\mathbf{B} \parallel \hat{\mathbf{z}}$, where $\hat{\mathbf{z}}$ is the unit vector pointing in the z-direction, simply gives $2A\cos^2\zeta\, \partial_z^2\psi = 0$, where $\partial_{x_i}^n$ refers to the nth partial derivative with respect to the spatial coordinate x_i. This has solutions $\psi(z) = k_0 + k_1 z$. Substituting this back into Equation (1), and evaluating the resultant indefinite integral, gives $E = z(Ak_1^2\cos^2\zeta - Dk_1\cos^2\zeta - B_S\sin\zeta)$ to within a constant. It can be minimized with respect to k_1 and ζ by elementary means, giving $k_1 = D/2A$ and $\zeta = \sin^{-1}(2BM_SA/D^2)$. This is the typical formulation of the conical phase with wavevector k_1 and tilt-angle ζ.

The CSL phase can be formulated analytically by orienting the magnetic field such that it is normal to the propagation vector of the helicoid. The field can then be used to orient the x-axis, so that $\mathbf{B} \parallel \hat{\mathbf{x}}$. This leads to an integrand that is more algebraically complicated, but widely studied[17,18]; the Euler–Lagrange equations of the free energy in this case give the time independent sine-Gordon equation, which has solitonic solutions[33]
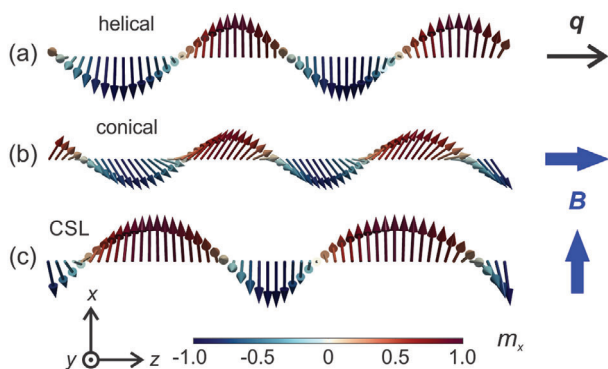
$$\sin\left(\frac{\psi(z) - \pi}{2}\right) = \text{sn}\left(\frac{\sqrt{B}}{\kappa}z \middle| \kappa\right) \quad (3)$$

where $\text{sn}(x|\kappa)$ is the Jacobi elliptic function with elliptic modulus κ. The energetically favorable value of κ is given by

$$\frac{\pi D}{2A\sqrt{\beta}} = \frac{e(\kappa)}{\kappa} \quad (4)$$

where $\beta = BM_S/\sqrt{A^2/4 + D^2}$ and $e(\kappa)$ is the complete elliptic integral of the second kind. Derivations of the detailed internal structure of magnetic solitons can be found in, e.g., Refs. [18, 34], but for convenience, graphical representations of both the CSL state and the conical state are provided in **Figure 1**.

The reason why experimental measurements of the CSL are so scarce is that the CSL and conical states both arise from the helical state under the influence of an external magnetic field. The only difference between the two states is geometric, with one requiring a field parallel to the helical propagation vector and the other requiring a perpendicular field. If the energy density of the

**ADVANCED
SCIENCE NEWS**

www.advancedsciencenews.com

**ADVANCED
PHYSICS
RESEARCH**
Open Access

www.advphysicsres.com

Figure 1. Visualization of the magnetic phases in a chiral magnets. a) Helical, b) conical, and c) CSL magnetization states, where magnetic moments are represented by arrows colored by their x-component.

conical state is lower than the energy density of the CSL, the helicoids can simply reorient themselves so that their propagation vector is parallel to the external field. Of course, this is impossible if intermediate states have a very high energy (which would

lead to there being a large energy barrier between the CSL and the conical state). Further, it is important to note that the most common technique for the observation of complex magnetic patterns is Lorentz transmission electron microscopy—a technique that does not generally allow for the application of magnetic vector fields. As the field can only be applied along the optical axis, the selection of materials is limited as discussed in the following.

To prevent solitons from reorienting and forming cones, previous measurements of the CSL have been taken on either uniaxial chiral magnets (such as $CrNb_3S_6$[7,8,35]), or on uniaxially strained cubic magnets.[23] The broken symmetry in these materials pins helicoidal structures such that they can propagate only along one specific direction.

Recently, Burn et al.[36] have reported the observation of a CSL phase in a ≈200-nm-thick plate of the cubic chiral magnet FeGe (with a T_C of ≈278 K slightly below room temperature). By applying an out-of-plane field, they identified the CSL state via the field-dependent behavior of its period, which is described by the 1D sine-Gordon model. The CSL was shown to exist over the entire probed temperature range from 268 to 273 K, over which the CSL period did not change. However, due to the out-of-plane ap-
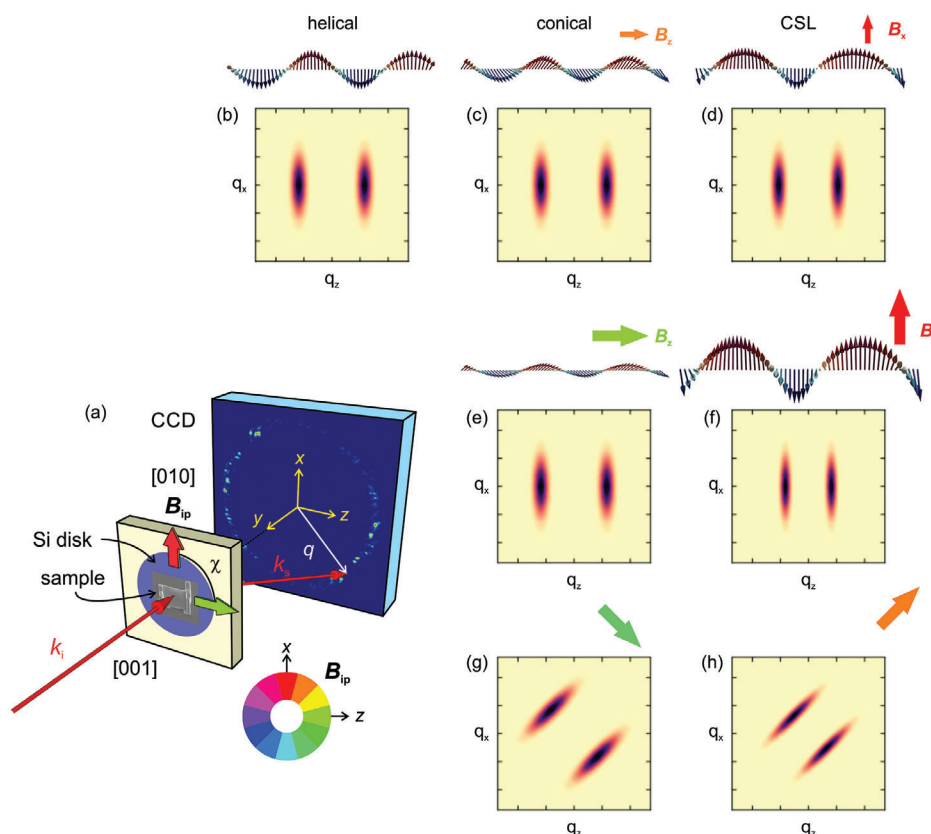
Figure 2. Magnetic phases in $Co_8Zn_{10}Mn_2$ and their T-REXS diffraction patterns. a) Illustration of the setup, showing the incoming (k_i) and scattered (k_s) X-rays, the $Co_8Zn_{10}Mn_2$ thin plate sample on the Si disk, the applied in-plane field directions (in-plane angle χ with respect to the crystallographic [010] direction (parallel to x-direction); [001] is normal to the surface (parallel to y-direction)), and the expected diffraction patterns for the respective idealized real-space structures (scattering vector **q**) on the CCD detector. For in-plane fields in $Co_8Zn_{10}Mn_2$, the helical, conical, and CSL phase can be observed. b-h) Illustrations of the magnetically ordered state (above) and the corresponding exaggerated diffraction pattern (of the quasi-1D state in the q_z-q_x plane; below). In the top row, the low field behavior is shown, and below the higher field behavior with the fields along z/x, and rotated by 45°. b) Helical state at zero (or very low) field. c) Conical state for $B\|z$ and d) CSL for $B\|x$. e,f) Same as in (c,d) for higher fields. g) Conical and h) CSL state for rotated in-plane fields as indicated. Note the differences in the peak separations for the CSL.

**ADVANCED
SCIENCE NEWS**

www.advancedsciencenews.com

**ADVANCED
PHYSICS
RESEARCH**
Open Access

www.advphysicsres.com

plication of the field, there was a phase competition between the CSL and other phases.

Here, we make use of one of the key advantages of X-ray based probes over electron beam based ones, i.e., the ability to apply fields in any direction. By exploring in-plane fields, which still fulfill the requirement for CSLs of the applied field being perpendicular to the helical propagation vector, we identified universal conditions for the stabilization of a robust CSL in the application-relevant, high temperature chiral magnet $Co_8Zn_{10}Mn_2$.

2.2. Reciprocal Space Mapping of the Magnetic Phases in a Chiral Magnet

For studying the magnetic states in a thin plate of a chiral magnet, we employ resonant elastic X-ray scattering (REXS) in transmission (T-REXS). With the X-ray energy tuned to the L_3 absorption edge of Co, T-REXS is probing the magnetic order of $Co_8Zn_{10}Mn_2$. Fields of up to 140 mT were applied in out-of-plane (y axis) and arbitrary in-plane (xz plane) directions, using a 3D vector field electromagnet (see **Figure 2**). The magnetic diffracted peaks were recorded with a CCD camera placed behind the sample. Note that as a reciprocal space imaging technique, T-REXS is particularly well-suited to probe magnetic correlations, which are only indirectly accessible in magnetometry and real-space imaging techniques.

In our $Co_8Zn_{10}Mn_2$ sample, there exist three magnetically ordered phases, the helical phase at zero (or low) field, the conical phase at higher fields, as well as the CSL phase. The expected diffraction patterns for these phases under different field directions and strengths is illustrated in Figure 2. In the top row, the case of small in-plane fields is shown for (b) the helical phase, (c) the conical phase (field along the z direction), and (d) the CSL phase ($B\|x$). In general, the appearance of the CSL phase is preceded by a loss in intensity of the helical phase (showing two magnetic peaks, i.e., the Friedel pair at $+\mathbf{q}$ and $-\mathbf{q}$). The CSL phase is characterized by two peaks at closer distance, which can be understood as the diffraction from a wider twist spacing. In principle, one can expect the occurrence of higher harmonics for the CSL,[23] i.e., diffraction spots at $2q$, $3q$, etc., however, due to the sample-detector distance being optimized for high q resolution, these spots are not observable in our setup. In the middle row, the diffraction patterns for larger in-plane fields are shown, where the effect on (f) the CSL peaks [in comparison to the conical peaks (e)] is particularly clear. Below, the case of rotated in-plane fields is illustrated, with both the (g) conical and (h) CSL phase peaks following the applied field direction. It is worth pointing out that we exploited the magnetic hysteresis of the sample to obtain temperature-stable, rotatable solitons. This was done by creating the perfect conditions for the helical state in the material and then applying a CSL-generating magnetic field.
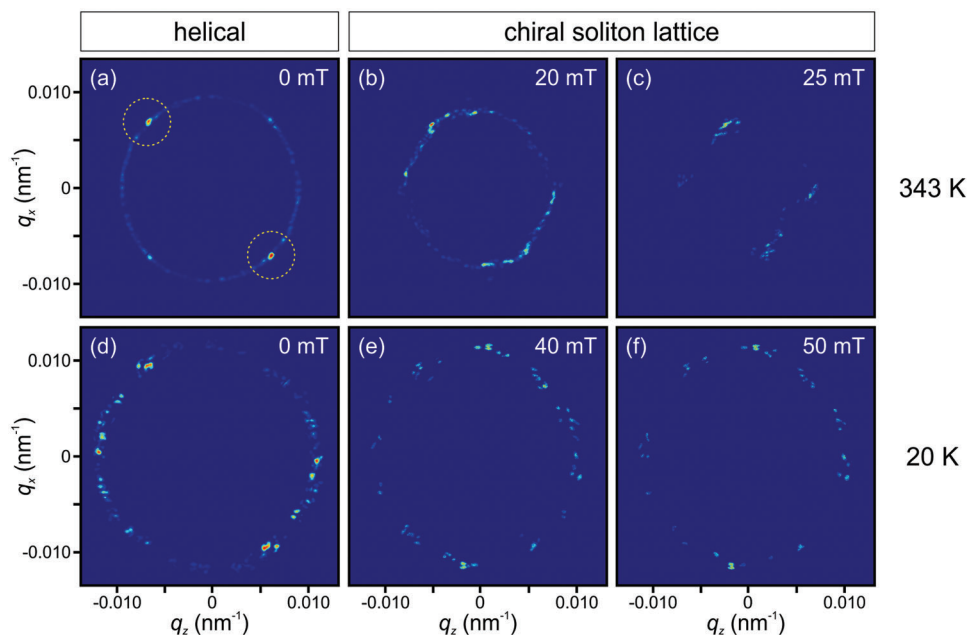
2.3. Reciprocal Space Mapping of the CSL

To generate an initial helical state with an arbitrary in-plane orientation, defining [001] as the out-of-plane direction, a magnetic field large enough to field-polarize the magnetization was applied at an azimuthal angle χ from the [010]-direction. For in-plane
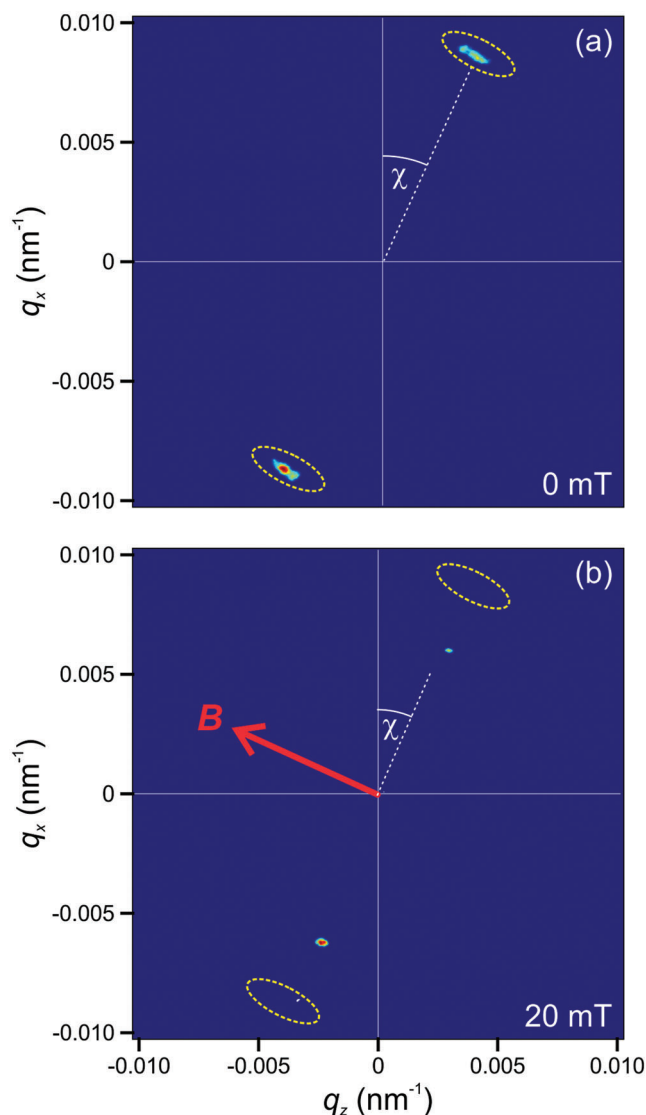
Figure 3. Relationship between field and scattering vector. a) A large magnetic field was applied χ degrees from the vertical (at 25.5° in this example), field polarizing the sample. The field was then slowly decreased to 0 mT. The propagation vector of the resultant helical state, at remanence, remained parallel to the direction of the previously applied magnetic field. b) The magnetic field was then slowly increased perpendicular to the helical propagation vector, which led to the formation of the CSL. This image was captured at 20 mT; the locations of the helical peaks from (a) are denoted by white dots.

fields, 100 mT was sufficient to field-polarize the magnetization at all measured temperatures. The field was then decreased to 0 mT. Decreasing the field to zero in this way will inevitably involve passing through a conical state whose propagation vector is parallel to the applied field. When the applied field becomes sufficiently small, the conical tilt angle $\zeta = 0°$, but the resultant helices inherit the conical orientation and have a propagation vector approximately an angle χ from the [010]-direction. An example of the application of this procedure with $\chi = 25.5°$ is shown in **Figure 3**a. All CCD images were processed using a local-stats module in python. Note that in other chiral crystals, magnetic

ADVANCED
SCIENCE NEWS

www.advancedsciencenews.com

ADVANCED
PHYSICS
RESEARCH
Open Access

www.advphysicsres.com

Figure 4. Reciprocal space images showing azimuthal maps of the CSL for different temperatures and fields. a-c) Averages of the scattering pattern from the CSL state across 120 equally spaced values of χ at 343 K at 0, 20, and 25 mT, respectively. d-f) Averages of the scattering pattern from the CSL state across 22 values of χ at 20 K at 0, 40, and 50 mT, respectively. At 343 K, the helical phase shows predominantly one domain (i.e., one pair of diffraction spots as indicated by yellow dotted circles), with the propagation vector aligned along a direction with $\chi \approx 45°$. A fainter pair of spots is visible in the perpendicular orientation, indicative of a second domain, which is to be expected owing to the cubic symmetry of the crystal.

anisotropies may be large enough to force helices to propagate parallel to certain crystallographic directions at remanence; this was not found to be the case in $Co_8Zn_{10}Mn_2$.

To prompt the formation of the CSL from the above-described initial state, a magnetic field was applied at an angle $\chi + 90°$ from the [010] direction, increasing from 0 up to 100 mT in steps of 1 mT. An example CSL scattering pattern obtained with $\chi = 25.5°$ and $|\mathbf{B}| = 20$ mT is shown in Figure 3b. For comparison, the location of the helical scattered intensity obtained at remanence is also shown in Figure 3b.

At a temperature of 343 K, this procedure was used to study the soliton state as a function of in-plane angle, varying χ from 0 to 180° in steps of 1.5°. An average over every value of χ at remanence is shown in **Figure 4**a. Further averages over every value of χ at 20 and 25 mT are shown in Figure 4b-c. An almost-equivalent experiment was carried out at 20 K, but with only 22 different values of χ. The results of the 20 K experiment can be found in Figure 4d-f. The data were collected in 1 mT steps, from 0 to 30 mT at 343 K, and from 0 to 55 mT at 20 K.
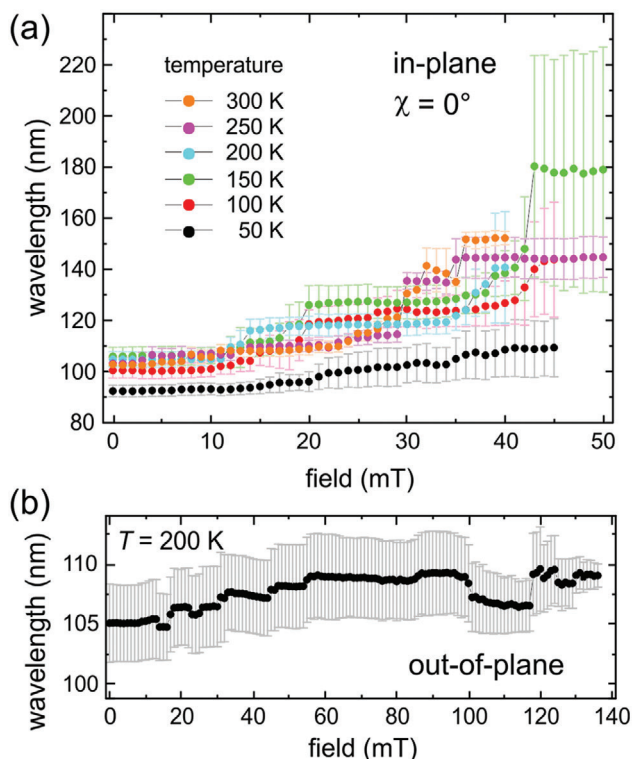
To obtain a measure of the wavelength $\lambda(|\mathbf{B}|)$, the images displayed in Figure 4, along with the images obtained at all other fields, were integrated in azimuthal slices using the pyFAI python package.[37] At temperatures of 300, 250, 200, 150, 100, 50, and 15 K, a single field sweep was carried out at $\chi = 0°$. The results of all field sweeps can be seen in **Figure 5**a. For comparison with the in-plane field data, $\lambda(|\mathbf{B}|)$ at 200 K with the magnetic field applied out-of-plane can be found in Figure 5b. The result of these integrations applied to the data collected at 343 K can be seen in **Figure 6**a, and the 20 K results are shown in Figure 6b.

Previous measurements of magnetic structure in thin plates of Co-Zn-Mn alloys, and other thin plates of chiral magnets, do

not typically show such solitonic behavior. We believe that this is because experimentalists typically apply **B** in an out-of-plane geometry.

2.4. Discussion

In T-REXS, the periodicity of the modulated structures is tracked as a function of applied field, finding that the length of the scattering vector **q** of the scattered X-rays is decreasing monotonically. This decrease was found to be clear and significant, and is easily visible in Figure 3b. The corresponding real-space periodicities (taken from Figure 6a) were calculated and the wavelength of the helices at remanence were found to be (104 ± 2.5) nm, increasing on average to a maximum of (158 ± 4.5) nm at 29 mT. The measured state transitions smoothly to and from the helical state, and does so only when the magnetic field is applied normal to the propagation vector of the helix. This behavior is unique to the CSL. Note that the $Co_8Zn_{10}Mn_2$ sample was mounted with the [100] direction out of plane, giving two symmetry equivalent [010] and [001] directions in the plane of the sample. This sample of $Co_8Zn_{10}Mn_2$ is a thin plate that has been transplanted over an aperture, as is required for T-REXS experiments. It is possible that the $Co_8Zn_{10}Mn_2$ plate has been unintentionally strained by this sample preparation procedure. However, as reported in Ref. [23], the magnitude of the helical scattering vector in Cu_2OSeO_3 was significantly affected by the controlled application of strain required to nucleate the chiral soliton phase, with the **q** vector further firmly locked along the strain direction. In our $Co_8Zn_{10}Mn_2$ sample, this is not the case, with the helical period at remanence of 104 nm agreeing reasonably well with that of other

**ADVANCED
SCIENCE NEWS**

www.advancedsciencenews.com

**ADVANCED
PHYSICS
RESEARCH**
Open Access

www.advphysicsres.com

Figure 5. Plots of the CSL wavelength as a function of temperature and field. Error bars represent the range of measured wavelengths. a) Maps of the soliton wavelength as a function of applied in-plane field and temperature, acquired using the recipe detailed in Figure 3, using $\chi = 0°$. (b) For comparison, an example of the dependence of helical wavelength on applied out-of-plane field. Note the different wavelength scale.

$Co_8Zn_{10}Mn_2$ samples, and, most importantly, with **q** not being locked in a particular direction. (Note that the value of the helical wavelength is strongly affected by the precise stoichiometry of the sample,[38] ranging from 100 to 200 nm).

It is also worth emphasizing that no attempt has been made to fit the experimentally measured $\lambda(\mathbf{B})$ to theoretical values. The error bars shown in Figure 5a are sufficiently large that any reasonable function could fit within them. While the data was qualitatively reproducible, the quantitative values of $\lambda(\mathbf{B})$ were dictated by pinning. The large size of the error bars in Figures 5 and 6 comes from the fact that multiple soliton domains were often simultaneously present. The occurrence of domains upon cooling can be attributed to the existence of competing interactions which become dominant at lower temperatures, starting to dominate over the symmetric exchange interaction. This behavior has been reported to be common in the Co-Zn-Mn compounds,[30,39] which hinder a meaningful theoretical analysis.

While it was possible to stabilize the CSL state with an arbitrary in-plane propagation vector, the experimentally measured $\lambda(\mathbf{B})$ displays an interesting dependency on azimuthal angle χ near T_C, as can be seen in Figure 4b,c. We associate this with the shape of the underlying thin plate. Solitons propagating along the longer diagonals of the thin plate have scattering vectors that appear on the diagonals of Figure 4c. These are significantly smaller on average than scattering vectors measured from the CSL that
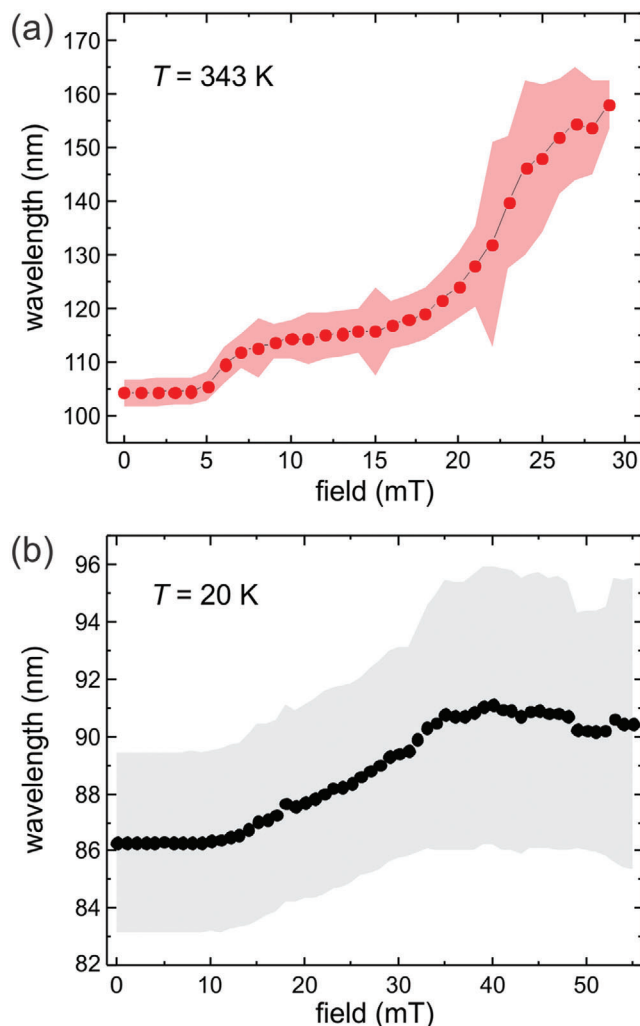
Figure 6. Averages over the anisotropy maps showing the CSL wavelength as a function of field for 343 and 20 K. a) The same data set as in Figure 4a-c, integrated in azimuthal slices about the central $\mathbf{q} = 0$ pixel to calculate CSL wavelength as a function of field. b) The same data set as in Figure 4d-f, integrated in azimuthal slices about the central $\mathbf{q} = 0$ pixel to calculate CSL wavelength as a function of field.

was propagating vertically/horizontally through the thin plate. It is worth noting that this effect is unlikely to be the consequence of underlying crystallographic anisotropies, as any anisotropic distortions of the solitonic propagation vectors would also be present at remanence in the helical state.

A striking difference between the anisotropy maps carried out at 343 and 20 K is the difference in helical wavelength at remanence; this can be seen as a function of temperature in Figure 5a. These data indicate that the reduction in helical wavelength is continuous, starting at around 100 K, making it unlikely that this is the result of a single structural or magnetic phase transition. This supports the findings of Ref. [26], where the authors saw a continuous change in the magnetization of $Co_8Zn_{10}Mn_2$ below 100 K. A detailed investigation of the helical wavelength of $Co_8Zn_{10}Mn_2$ as a function of temperature would be an interesting and important further study.

**ADVANCED
SCIENCE NEWS**

www.advancedsciencenews.com

**ADVANCED
PHYSICS
RESEARCH**
Open Access

www.advphysicsres.com

Another clear difference is that the wavelength of solitons at 20 K does not increase as much with field as at 343 K. This trend is visible in Figure 6b: the soliton wavelength increases less freely as a function of applied field the further the temperature is from T_C. This is not surprising as it is clear from the temperature dependence of the helical wavelength in Figure 5a that the magnetic properties of the sample are a function of temperature.

Finally, the application of an out-of-plane magnetic field did not produce solitons at any temperature. We expect that the demagnetizing field from the highly anisotropic thin plate plays an important role in stabilizing the CSL.

3. Conclusion

We have taken extensive measurements of the CSL state from above room temperature to 15 K. We have shown that the CSL can be stabilized with a propagation vector in an arbitrary in-plane direction in $Co_8Zn_{10}Mn_2$. We attribute anisotropy in the resultant azimuthal map to the rectangular shape of the $Co_8Zn_{10}Mn_2$ thin plate. The data collected demonstrate a significant increase in pinning of the magnetization field at low temperatures. Our results are significant as they constitute the first observation of the CSL state above room temperature. This high temperature brings the CSL state an important step closer to its adoption in computing devices. Secondly, as $Co_8Zn_{10}Mn_2$ belongs to the $P4_132$ space group, and as it is not a uniaxial magnet like $CrNb_3S_6$ and $Yb(Ni_{1-x}Cu_x)_3Al_9$, the CSL state follows the applied in-plane field direction, providing design flexibility. Our work therefore opens the door to above room temperature solitonic applications.

4. Experimental Section

Sample Preparation: $Co_8Zn_{10}Mn_2$ single crystals were grown by the Bridgman method.[26] $Co_8Zn_{10}Mn_2$ single crystals were then extracted from the as-grown boule, and oriented using X-ray Laue backscattering. The magnetic properties of the $Co_8Zn_{10}Mn_2$ crystals were determined using an MPMS3 vibrating sample magnetometer, measuring a Curie temperature of 365 K. Focused ion beam (FIB) milling was used to prepare a thin lamella of the material, measuring 10 μm×10 μm×400 nm. It was was then put in place with a micromanipulator onto a Si_3N_4 membrane with a 6-μm-diameter aperture on a Si disk, and secured using FIB-based Pt deposition.

Transmission Resonant Elastic X-Ray Scattering: The experiment was carried out on beamline I10 at Diamond Light Source, using the portable octupole magnet (POMS) end-station. POMS is capable of providing 3D magnetic vector fields of up to 0.8 T at temperatures down to ≈10 K. Resonant elastic X-ray scattering was performed in a transmission geometry (T-REXS) on the L_3 edges of Co, Zn, and Mn of a 400-nm-thick $Co_8Zn_{10}Mn_2$ lamella using positive circularly polarized light under ultra-high vacuum conditions. (For reference, both circular polarizations were tested). With the X-ray energy tuned to the L_3 absorption edge of an element in the compound, T-REXS is probing the out-of-plane magnetic order associated with that element. For $Co_8Zn_{10}Mn_2$, we explored the L_3 edges of Co (778.1 eV), Zn (1021.8 eV), and Mn (638.7 eV) and found that Co and Mn show identical magnetic behavior, while Zn shows no magnetic signal. The magnetic diffraction peaks were recorded on a CCD camera mounted to POMS at a distance of 474 mm from the sample. A beam stop is used to protect the camera by blocking out the straight-through beam. Given the capabilities of POMS, full phase maps can be obtained, not only as a function of applied field and temperature, but also as a function of field direction.

Conflict of Interest

The authors declare no conflict of interest.

Data Availability Statement

The data that support the findings of this study are available from the corresponding author upon reasonable request.

[1] A. Fert, N. Reyren, V. Cros, *Nat. Rev. Mater.* **2017**, *2*, 17031.
[2] W. Wang, D. Song, W. Wei, P. Nan, S. Zhang, B. Ge, M. Tian, J. Zang, H. Du, *Nat. Commun.* **2022**, *13*, 1593.
[3] I. E. Dzyaloshinskii, *Sov. Phys. JETP* **1964**, *19*, 960.
[4] Y. A. Izyumov, *Sov. Phys. Usp.* **1984**, *27*, 845.
[5] J. ichiro Kishine, A. S. Ovchinnikov, *J. Phys. C* **2015**, *66*, 1.
[6] T. Higaki, K. Kamada, K. Nishimura, *Phys. Rev. D* **2022**, *106*, 096022.
[7] Y. Togawa, T. Koyama, K. Takayanagi, S. Mori, Y. Kousaka, J. Akimitsu, S. Nishihara, K. Inoue, A. Ovchinnikov, J.-i. Kishine, *Phys. Rev. Lett.* **2012**, *108*, 107202.
[8] Y. Togawa, Y. Kousaka, S. Nishihara, K. Inoue, J. Akimitsu, A. S. Ovchinnikov, J.-i. Kishine, *Phys. Rev. Lett.* **2013**, *111*, 197204.
[9] A. B. Borisov, J.-i. Kishine, I. G. Bostrem, A. S. Ovchinnikov, *Phys. Rev. B* **2009**, *79*, 134436.
[10] J.-i. Kishine, A. S. Ovchinnikov, I. V. Proskurin, *Phys. Rev. B* **2010**, *82*, 064407.
[11] V. Laliena, S. Bustingorry, J. Campo, *Sci. Rep.* **2020**, *10*, 20430.
[12] I. G. Bostrem, J.-i. Kishine, A. S. Ovchinnikov, *Phys. Rev. B* **2008**, *78*, 064425.
[13] J.-i. Kishine, I. V. Proskurin, A. S. Ovchinnikov, *Phys. Rev. Lett.* **2011**, *107*, 017205.
[14] M. N. Wilson, E. A. Karhu, D. P. Lake, A. S. Quigley, S. Meynell, A. N. Bogdanov, H. Fritzsche, U. K. Rößler, T. L. Monchesky, *Phys. Rev. B* **2013**, *88*, 214420.
[15] Y. Togawa, Y. Kousaka, K. Inoue, J.-i. Kishine, *J. Phys. Soc. Jpn.* **2016**, *85*, 112001.
[16] F. J. T. Goncalves, Y. Shimamoto, T. Sogo, G. W. Paterson, Y. Kousaka, Y. Togawa, *Appl. Phys. Lett.* **2020**, *116*, 012403.
[17] J.-i. Kishine, K. Inoue, Y. Yoshida, *Prog. Theor. Phys. Suppl.* **2005**, *159*, 82.
[18] P. G. De Gennes, *Sol. State Commun.* **1968**, *6*, 163.
[19] C. Zhang, J. Zhang, C. Liu, S. Zhang, Y. Yuan, P. Li, Y. Wen, Z. Jiang, B. Zhou, Y. Lei, D. Zheng, C. Song, Z. Hou, W. Mi, U. Schwingenschlögl, A. Manchon, Z. Q. Qiu, H. N. Alshareef, Y. Peng, X.-X. Zhang, *Adv. Mater.* **2021**, *33*, 2101131.

[20] S. Mühlbauer, B. Binz, F. Jonietz, C. Pfleiderer, A. Rosch, A. Neubauer, R. Georgii, P. Böni, *Science* **2009**, *323*, 915.

[21] D. A. Mayoh, J. Bouaziz, A. E. Hall, J. B. Staunton, M. R. Lees, G. Balakrishnan, *Phys. Rev. Res.* **2022**, *4*, 013134.

[22] A. E. Hall, J. C. Loudon, P. A. Midgley, A. C. Twitchett-Harrison, S. J. R. Holt, D. A. Mayoh, J. P. Tidey, Y. Han, M. R. Lees, G. Balakrishnan, *Phys. Rev. Mater.* **2022**, *6*, 024407.

[23] Y. Okamura, Y. Yamasaki, D. Morikawa, T. Honda, V. Ukleev, H. Nakao, Y. Murakami, K. Shibata, F. Kagawa, S. Seki, T. Arima, Y. Tokura, *Phys. Rev. B* **2017**, *96*, 174417.

[24] X. Z. Yu, Y. Onose, N. Kanazawa, J. H. Park, J. H. Han, Y. Matsui, N. Nagaosa, Y. Tokura, *Nature* **2010**, *465*, 901.

[25] X. Z. Yu, N. Kanazawa, Y. Onose, K. Kimoto, W. Z. Zhang, S. Ishiwata, Y. Matsui, Y. Tokura, *Nature Mater.* **2011**, *10*, 106.

[26] Y. Tokunaga, X. Z. Yu, J. S. White, H. M. Rønnow, D. Morikawa, Y. Taguchi, Y. Tokura, *Nat. Commun.* **2015**, *6*, 7638.

[27] W. Xie, S. Thimmaiah, J. Lamsal, J. Liu, T. W. Heitmann, D. Quirinale, A. I. Goldman, V. Pecharsky, G. J. Miller, *Inorg. Chem.* **2013**, *52*, 9399.

[28] X. Z. Yu, W. Koshibae, Y. Tokunaga, K. Shibata, Y. Taguchi, N. Nagaosa, Y. Tokura, *Nature* **2018**, *564*, 95.

[29] M. T. Birch, D. Cortes-Ortuno, K. Litzius, S. Wintz, F. Schulz, M. Weigand, A. Stefancic, D. A. Mayoh, G. Balakrishnan, P. D. Hatton, G. Schütz, *Nat. Commun.* **2022**, *13*, 3630.

[30] J. S. White, K. Karube, V. Ukleev, P. M. Derlet, R. Cubitt, C. D. Dewhurst, A. R. Wildes, X. Z. Yu, H. M. Rønnow, Y. Tokura, Y. Taguchi, *J. Appl. Cryst.* **2022**, *55*, 1219.

[31] M. Preißinger, K. Karube, D. Ehlers, B. Szigeti, H.-A. Krug von Nidda, J. S. White, V. Ukleev, H. M. Rönnow, Y. Tokunaga, A. Kikkawa, Y. Tokura, Y. Taguchi, I. Kézsmárki, *npj Quantum Mater.* **2021**, *6*, 65.

[32] R. Brearton, Ph.D. thesis, University of Oxford, **2021**.

[33] J. Rubinstein, *J. Math. Phys.* **1970**, *11*, 258.

[34] M. J. Ablowitz, D. J. Kaup, A. C. Newell, H. Segur, *Phys. Rev. Lett.* **1973**, *30*, 1262.

[35] T. Honda, Y. Yamasaki, H. Nakao, Y. Murakami, T. Ogura, Y. Kousaka, J. Akimitsu, *Sci. Rep.* **2020**, *10*, 18596.

[36] D. M. Burn, S. L. Zhang, S. Wang, H. F. Du, G. van der Laan, T. Hesjedal, *Phys. Rev. B* **2019**, *100*, 184403.

[37] G. Ashiotis, A. Deschildre, Z. Nawaz, J. P. Wright, D. Karkoulis, F. E. Picca, J. Kieffer, *J. Appl. Crystallogr.* **2015**, *48*, 510.

[38] J. D. Bocarsly, C. Heikes, C. M. Brown, S. D. Wilson, R. Seshadri, *Phys. Rev. Mater.* **2019**, *3*, 014402.

[39] K. Karube, J. S. White, V. Ukleev, C. D. Dewhurst, R. Cubitt, A. Kikkawa, Y. Tokunaga, H. M. Rønnow, Y. Tokura, Y. Taguchi, *Phys. Rev. B* **2020**, *102*, 064408.